

Matrix optimization on universal unitary photonic devices

Sunil Pai,^{1,*} Ben Bartlett,² Olav Solgaard,¹ and David A. B. Miller^{1,†}

¹*Department of Electrical Engineering, Stanford University, Stanford, CA 94305, USA*

²*Department of Applied Physics, Stanford University, Stanford, CA 94305, USA*

Universal unitary photonic devices are capable of applying arbitrary unitary transformations to multi-port coherent light inputs and provide a promising hardware platform for fast and energy-efficient machine learning. We address the problem of training universal photonic devices composed of meshes of tunable beamsplitters to learn unknown unitary matrices. The locally-interacting nature of the mesh components limits the fidelity of the learned matrices if phase shifts are randomly initialized. We propose an initialization procedure derived from the Haar measure over unitary matrices that overcomes this limitation. We also embed various model architectures within a standard rectangular mesh “canvas,” and our numerical experiments show significantly improved scalability and training speed, even in the presence of fabrication errors.

I. INTRODUCTION

Universal unitary photonic devices are capable of performing arbitrary unitary transformations on input vectors of coherent light modes. Such devices serve important applications, including quantum computing (e.g. boson sampling) [1–3] and mode unscramblers [4]. When two unitary photonic devices are combined with gain or attenuation elements, the resulting singular value decomposition architecture can efficiently perform arbitrary linear operations [5]. These architectures are useful for implementing photonic neural networks [6] and finding optimal channels through lossy scatterers [7].

The most common photonic implementations of devices that perform such unitary operations involve waveguide circuits composed of 50 : 50 beamsplitters (such as directional couplers) and phase shifters arranged in grid meshes [5, 6, 8–10]. In waveguide circuits, the N -dimensional input vector is represented by an array of modes arranged in N single-mode input waveguides. Rather than perform a single operation on all inputs, universal unitary photonic devices perform a sequence of pairwise operations on light inputs using Mach-Zehnder interferometers (MZIs) shown in Figure 1(a, b). In the photonic MZI shown in Figure 1(b), directional couplers allow for interaction between waveguide modes, and phase shifters tune the phases and relative amplitudes of the output modes of the interferometer. These devices are universal in the sense that they can theoretically be configured to perform any unitary operation (and by extension, any linear operation [5]).

Three architectures have been proposed for such meshes: “triangular” [5, 8], “cascaded binary tree” [11], and “rectangular” [9]. All of these are “forward-only architectures”—light only propagates in one direction—which can simplify progressive setup. (Such architectures can also be embedded in non-forward-only meshes [12–14].) Using progressive algorithms [5, 11], the triangular

and binary tree architectures can be progressively configured maximizing power at output detectors using a minimum number of training vectors.

These architectures also support “self-configuration,” in which they can automatically separate orthogonal input vectors, performing self-aligning beam coupling [11] and separation of scrambled modes [4]. With monitors embedded in each MZI block, such separation can adapt continuously to environmental drift [4, 5, 11]. The rectangular mesh does not support self-configuration nor progressive setup based on output detectors alone, but it is shorter than the triangular mesh and has other benefits such as symmetry [9, 15]. With embedded monitors at each MZI, the rectangular mesh could be progressively configured with either a more complex algorithm [9, 16] or global multi-parameter optimization [17].

Imperfections in the components of the MZI mesh is an issue with all such architectures. In particular, the beamsplitting ratios may not be exactly 50 : 50, which makes it difficult to obtain high MZI rejection (i.e., small or large reflectivities or overall split ratios). Especially in large meshes, it has been noted that many of the MZIs are required to have low reflectivities [18]. One way of achieving low reflectivities is to use additional (and imperfect) MZIs as beamsplitters [19, 20]. This double-MZI approach doubles the number of beamsplitters in the overall mesh, but achieves substantial improvement in performance [20]. This approach can be combined with progressive configuration algorithms to implement high fidelity unitary matrices in large meshes [16, 19].

Global multi-parameter optimization is an alternative approach to configuring meshes and compensating for imperfections. This approach can also be extended to machine learning, where the system is fed training data to learn to perform a desired function such as classifying images or recognizing speech. In this context, the unitary matrix that performs the mapping is *unknown*, and must therefore be learned from the input and target data represented by the input and output modes of the system, respectively. By contrast, a self-configuring mesh implements a *known* matrix or unscrambles *known* modes [4].

* sunilpai@stanford.edu

† dabm@stanford.edu

In situ backpropagation is one example of global optimization that can be performed using photodetector measurements [17]. Backpropagation is relevant to photonic neural networks [6] and possibly quantum machine learning [15, 21, 22] using universal photonic devices. While quantum machine learning algorithms may optimize a single unitary mesh to learn decision or encoding functions [21], a classical photonic deep neural network approach uses backpropagation over many stacked unitary meshes to learn such functions [17].

In this paper, we simulate training of phase shifters in a photonic mesh to learn a unitary operation. This on-chip matrix optimization process, unlike progressive self-configuration, is not necessarily achievable in polynomial time. Unlike conventional computers that train the matrix elements via linear optimization, the photonic mesh trains matrix elements via a non-convex optimization of phase shifter settings. Photonic matrix optimization is thus fundamentally different from conventional linear matrix optimization, and it warrants in-depth study, especially for photonic neural networks.

Unitary operators trained using photonic matrix optimization have errors that increase with the element-wise distance from the diagonal. Off-diagonal, “non-local” matrix elements correspond physically to transitions between input and output waveguides that are far apart vertically in Figure 1(c, d), and for which there is only a small number of possible paths connecting them through the mesh. As a result, these connections have increased sensitivity to calibration and fabrication errors along those paths. Concomitantly, phase shifters at the center of the mesh affect an increased number of inputs and outputs (and thus have lower error tolerances) than those near the boundary of the mesh. It should be noted that this characteristic is relevant to the error analysis of both self-configuration and optimization algorithms for photonic meshes.

We propose a simple protocol, which we call “Haar initialization,” to improve the convergence of photonic backpropagation for on-chip matrix optimization. We also propose two alterations to the rectangular mesh that significantly improve matrix optimization performance and can be tested when embedded in a rectangular mesh “canvas.” First, we coarse-grain the mesh interactions while maintaining the same number of tunable components. Coarse-graining increases required tolerances of phase shifters, decreases off-diagonal errors, and decreases convergence time. Second, adding redundancy through extra tunable layers to the mesh improves overall convergence to machine precision.

II. PHOTONIC MESH THEORY

A. Photonic unitary implementation

A single-mode phase shifter can perform an arbitrary $U(1)$ transformation $e^{i\phi}$ on its input. A phase-modulated

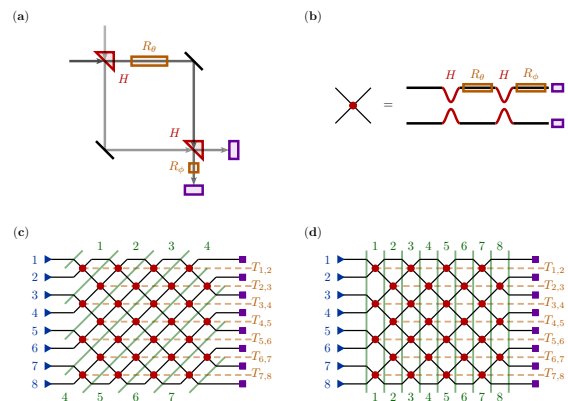


FIG. 1. (a) Bulk optics MZI vs (b) Photonic MZI with 50:50 beamsplitters H (red), phase shifters R_θ, R_ϕ (orange), and detectors (purple). (c, d) Diagrams representing the locally interacting rectangular decomposition for $N = 8$. The inputs (and single-mode phase shifts at the inputs) are represented by blue triangles. Outputs are represented by purple squares. The MZI nodes are represented by red dots. The Givens rotations (orange lines) can either be defined using ordered layers (diagonal green lines, c) where rotations must be applied left to right within the layer, or commuting layers (vertical green lines, d) where rotations can be applied in any order within the layer.

Mach-Zehnder interferometer (MZI) with perfect (50 : 50) beamsplitters can apply to its inputs a unitary transformation U of the form:

$$\begin{aligned}
 U(\theta, \phi) &= HR_\theta HR_\phi \\
 &= \frac{1}{\sqrt{2}} \begin{bmatrix} 1 & 1 \\ 1 & -1 \end{bmatrix} \begin{bmatrix} e^{i\theta} & 0 \\ 0 & 1 \end{bmatrix} \frac{1}{\sqrt{2}} \begin{bmatrix} 1 & 1 \\ 1 & -1 \end{bmatrix} \begin{bmatrix} e^{i\phi} & 0 \\ 0 & 1 \end{bmatrix} \\
 &= e^{\frac{i\theta}{2}} e^{\frac{i\phi}{2}} \begin{bmatrix} e^{\frac{i\phi}{2}} \cos \frac{\theta}{2} & ie^{-\frac{i\phi}{2}} \sin \frac{\theta}{2} \\ ie^{\frac{i\phi}{2}} \sin \frac{\theta}{2} & e^{-\frac{i\phi}{2}} \cos \frac{\theta}{2} \end{bmatrix} \\
 &\equiv \begin{bmatrix} r & -t^* \\ t & r^* \end{bmatrix},
 \end{aligned} \tag{1}$$

where H, R_θ, R_ϕ are operators depicted in Figure 1, r is the reflectivity, and t is the transmissivity. (Note that we ignore the leading global phase terms $e^{\frac{i\theta}{2}} e^{\frac{i\phi}{2}}$.) This is equivalent to the configuration in the top right of Figure 1, but other configurations with two independent phase shifters in the MZI block are ultimately equivalent for photonic meshes [19]. If one or two single-mode phase shifters are added at the inputs, we can apply an arbitrary $SU(2)$ or $U(2)$ transformation to the inputs, respectively.

In our convention, when $\theta = \phi = 0$, we get the identity transformation where $r = 1, t = 0$ (the “bar state” of the MZI). When $\theta = \pi, \phi = 0$, we get the “flip” transformation where $r = 0, t = 1$ (the “cross state” of the MZI).

If there are N input waveguides and the interferometer is connected to waveguides m and m' (with $m < m'$),

then we can express the 2×2 unitary transformation embedded in the N -dimensional space of the waveguides with a unitary Givens rotation:

$$T_{m,m'} = \begin{matrix} & \begin{matrix} m & m' \end{matrix} \\ \begin{matrix} 1 & \cdots & 0 & \cdots & 0 & \cdots & 0 \\ \vdots & \ddots & \vdots & & \vdots & & \vdots \\ 0 & \cdots & r & \cdots & -t^* & \cdots & 0 \\ \vdots & & \vdots & \ddots & \vdots & & \vdots \\ 0 & \cdots & t & \cdots & r^* & \cdots & 0 \\ \vdots & & \vdots & & \vdots & \ddots & \vdots \\ 0 & \cdots & 0 & \cdots & 0 & \cdots & 1 \end{matrix} & \begin{matrix} m \\ m' \end{matrix} \end{matrix}, \quad (2)$$

where we show labels for the m and m' columns and rows. Note that all diagonal elements are 1 except $T_{m,m} = r$ and $T_{m',m'} = r^*$, and all off-diagonal elements are 0 except the elements $T_{m,m'} = -t^*$, $T_{m',m} = t$. If $m' = m + 1$, matrix elements r , $-t^*$, t , and r^* form a 2×2 block on the diagonal, and the Givens rotation is “locally interacting.”

Arbitrary unitary transformations can be implemented on a photonic chip using only locally interacting MZIs, which are straightforward to fabricate. Several decomposition schemes have been proposed for this, but in this paper we will specifically focus on optimizing the rectangular decomposition [9]. However, our ideas can be extended to other schemes, such as the triangular decomposition [5], as well.

In the rectangular decomposition (RD) scheme [9], we represent $U_{\Pi} \in \text{U}(N)$ in terms of $N(N-1)/2$ locally interacting Givens rotations $T_{m,m+1}$ and N single-mode phase shifts at the inputs represented by diagonal unitary $D(\gamma_1 \cdots \gamma_N)$:

$$\begin{aligned} U_{\Pi} &= D(\gamma_1 \cdots \gamma_N) \prod_{n=1}^N \prod_{m \in \mathcal{M}_{n,N}} T_{m,m+1}(\theta_{mn}, \phi_{mn}) \\ &= D(\gamma_1 \cdots \gamma_N) \prod_{n=1}^N U_{\Pi}^{(n)}(\theta_{mn}, \phi_{mn}), \end{aligned} \quad (3)$$

where the single-mode phase shifts are $\gamma_n \in [0, 2\pi)$, the Givens rotations are parametrized by $\theta_{mn} \in [0, \pi)$, $\phi_{mn} \in [0, 2\pi)$, and $\mathcal{M}_{n,N}$ are sequential integers $m \in [1, N-1]$ of the same parity as n . This definition follows the commuting layers definition [23] depicted in Figure 1(d), where n represents the index of the commuting layer. Note in our convention, we left-multiply $v_o^T = v_i^T U_{\Pi}$, where $v_i, v_o \in \mathbb{C}^N$ are input and output modes respectively. The commuting layers $U_{\Pi}^{(n)}$ apply transformations to the input left-to-right in Equation 3, corresponding to the sequential transformations of input mode vector v_i as it flows in the mesh from left to right until output mode vector v_o is detected.

B. Photonic unitary error tolerances

As mentioned in the introduction, when fabricating photonic beamsplitters, small changes in interaction length or coupling gap of directional coupler designs limits the transmissivity and reflectivity of the scattering matrix for the MZIs. We define ϵ as twice the displacement from 50% in measured split ratio after each directional coupler. For simplicity, we assume both of the transmission power errors in the directional couplers are identical. A scattering matrix incorporating these errors can be written as:

$$U_{\epsilon} = \begin{bmatrix} r_{\epsilon} & -t_{\epsilon}^* \\ t_{\epsilon} & r_{\epsilon}^* \end{bmatrix} \quad (4)$$

where $|t_{\epsilon}|^2 \equiv |t|^2(1 - \epsilon^2) \in [0, 1 - \epsilon^2]$ is the realistic transmissivity, $|r_{\epsilon}|^2 \equiv |r|^2 + |t|^2\epsilon^2 \in [\epsilon^2, 1]$ is the realistic reflectivity, and t, r are the ideal transmissivity and reflectivity defined in Equation 1.

We give a derivation for Equation 4 in Appendix A, and a more detailed error analysis with more stringent assumptions is provided in [19]. We use Equation 4 in our experiments to implement unconstrained optimization of a photonic mesh with beamsplitter errors.

Regardless of the photonic mesh architecture used for training, optimization suffers because the unitary matrices in Equation 4 cannot express the full range of $\text{U}(2)$ (since transmission amplitude $|t| \leq \sqrt{1 - \epsilon^2}$). Furthermore, as pointed out by the authors of [18], such errors also confound matrix construction algorithms. Our theory may enable one to determine acceptable tolerances for calibration of a “perfect mesh” consisting of imperfect directional coupler components [19].

III. HAAR PHASE

A. Haar measure

To quantify the tolerances needed to calibrate the mesh phases θ_{mn} throughout the rectangular mesh, we introduce the Haar measure $d\mu(U)$ [2, 24, 25]. The Haar measure on a locally compact group G is an invariant volume that is preserved under any parametrization of G . For example, the Haar measure for $\text{U}(2)$ is the invariant volume of the solid angle in spherical coordinates, $\sin \frac{\theta}{2} \cos \frac{\theta}{2} d\theta d\phi d\gamma_1 d\gamma_2$, where $\phi, \gamma_1, \gamma_2 \in [0, 2\pi)$ adjust common mode and differential mode phase shifts and $\theta \in [0, \pi]$ adjusts relative magnitude.

The Haar measure can be defined for $\text{U}(N)$ in two bases: the Cartesian basis dX and the phase basis $d\Theta d\Phi d\Gamma$ (the phase shifter values in the mesh,

$(\theta_{mn}, \phi_{mn}, \gamma_n)$:

$$\begin{aligned} dX &= \prod_{i=1}^{N^2} du_i \\ d\Theta d\Phi d\Gamma &= \prod_{m,n} d\theta_{mn} \prod_{m,n} d\phi_{mn} \prod_n d\gamma_n, \end{aligned} \quad (5)$$

where, as defined in [25], $U = \sum_i u_i V_i$ with V_i some orthogonal basis in $\mathbb{C}^N \times \mathbb{C}^N$ and $u_i = \text{Tr}(V_i^\dagger U) / \text{Tr}(V_i^\dagger V_i)$. Note that both differential volumes defined in Equation 5 have N^2 degrees of freedom. The Haar measure $d\mu(U)$ for a matrix U can be expressed in either of these bases as [25]

$$d\mu(U) = dX = \det \mathcal{J} d\Theta d\Phi d\Gamma. \quad (6)$$

Since $d\mu(U) = dX$, we refer to uniform randomness in u_i as ‘‘Haar random.’’ The Jacobian $\mathcal{J} \in \mathbb{C}^{N^2 \times N^2}$ defined in Equation 6 is found in [25], and more explicitly for photonic meshes in [2]. The invariant volume or Haar measure represents how changes in the parameters of the phase basis affect the Cartesian basis.

Since the phases ϕ_{mn}, γ_n can be varied uniformly without changing $\det \mathcal{J}$, then the determinant of the Jacobian that expresses $N(N-1)/2$ Cartesian magnitudes u_i in terms of $N(N-1)/2$ phases θ_{mn} is alone sufficient to find $\det \mathcal{J}$ [2, 25]. The $\det \mathcal{J}$ in the Haar measure is also the probability density function (PDF) for the phase basis necessary to generate a Haar random unitary matrix [2].

B. Haar phase

We now introduce the ‘‘Haar phase’’ ξ_{mn} , which we define as the cumulative density function (CDF) of $\theta_{mn}/2$:

$$\xi_{mn} = \int_0^{\theta_{mn}/2} \mathcal{P}_{\alpha_{mn}}(\theta) d\theta \quad (7)$$

where $\mathcal{P}_{\alpha_{mn}}$ represents the probability density function (PDF) of θ_{mn} for a Haar random unitary matrix for a given ‘‘Haar phase power term’’ α_{mn} , which we will discuss shortly. Note that since uniform ϕ_{mn}, γ_n is sufficient for Haar randomness, we need only parametrize θ_{mn} . The Haar measure $d\Xi$ parametrized by $\xi_{mn}(\theta_{mn})$ becomes

$$\begin{aligned} d\Xi &= \prod_{m,n} d\xi_{mn} = \det \mathcal{J} \prod_{m,n} d\theta_{mn} \\ dX &= \det \mathcal{J} d\Theta d\Phi d\Gamma = d\Xi d\Phi d\Gamma. \end{aligned} \quad (8)$$

By splitting up terms in the Jacobian determinant $\det \mathcal{J}$ in Equation 8, we arrive at a uniformly distributed parameter $\xi_{mn}(\theta_{mn}) \in [0, 1]$ that yields a Haar random

matrix:

$$\begin{aligned} \xi_{mn} &= \left[\sin\left(\frac{\theta_{mn}}{2}\right) \right]^{2\alpha_{mn}} \\ d\xi_{mn} &= \frac{1}{2} d\theta_{mn} \mathcal{P}_{\alpha_{mn}}(\theta_{mn}/2) \\ &= d\theta_{mn} \alpha_{mn} \cos\left(\frac{\theta_{mn}}{2}\right) \left[\sin\left(\frac{\theta_{mn}}{2}\right) \right]^{2\alpha_{mn}-1}, \end{aligned} \quad (9)$$

for a given Haar phase power term $\alpha_{mn} \in [1, \dots, N-1]$, which depends on the mesh architecture used and on (m, n) .

Using the ordered (diagonal) layer definition in Figure 1, Russell et al. calculate their ‘‘reduced’’ Jacobian and find a separable determinant of the same form as Equation 9. For the rectangular and triangular meshes, an intuitive and useful definition for the Haar phase power term is $\alpha_{mn} = |I_{mn}| + |O_{mn}| - N - 1$, where I_{mn} and O_{mn} are the subsets of input and output waveguides accessible by the MZI at (m, n) and $|\cdot|$ denotes set size. This definition is equivalent for both the triangular and rectangular decompositions to $\mathcal{P}(\theta_{mn}; \alpha_{mn})$ as derived in [2], which we prove inductively in Appendix E.

The standard deviation of $\theta/2$ can be expressed in terms of α as

$$\sigma_{\theta;\alpha} = \sqrt{\mathbf{E}_{\mathcal{P}_\alpha} \left[\left(\frac{\theta}{2} \right)^2 \right] - \left(\mathbf{E}_{\mathcal{P}_\alpha} \left[\frac{\theta}{2} \right] \right)^2}, \quad (10)$$

where $\mathbf{E}_{\mathcal{P}_\alpha}[\cdot]$ refers to the expected value for a quantity where $\theta/2$ is distributed according to the PDF \mathcal{P}_α . As shown in Figure 2(b), the standard deviation $\sigma_{\theta;\alpha_{mn}}$ decreases as α_{mn} increases. Therefore, a phase shifter’s allowable tolerance¹ decreases as the total number of input and output ports affected by that component increases. Since α_{mn} is $\mathcal{O}(N)$, the required tolerance gets more restrictive at large N as shown in Figure 2(c).

The zeroth order θ_{mn} term expanded around the Haar phase $\xi_\alpha = 0.5$ gives $\theta^{(0)}(\xi_\alpha)/2 = \arcsin \sqrt[2\alpha]{\frac{1}{2}}$, which approaches $\pi/2$ for large α . Therefore, as α_{mn} increases, the median value of $\theta/2$ shifts closer to $\pi/2$; in our convention, $\theta/2 = \pi/2$ corresponds to transmissive phase shifts. (By ‘‘transmissive’’ we mean that power at the top left input is transmitted to the bottom right output - the ‘‘cross’’ state of the MZI.) Since α_{mn} increases as it approaches the center of the mesh, the mesh is more transmissive at its center than at its boundary, allowing for better control of off-diagonal magnitudes. Since α_{mn} is $\mathcal{O}(N)$, the average phase shift for Haar randomness gets closer to $\pi/2$ at large N .

Note from Figure 2(a, b) that the derivative $\frac{d\xi}{d\theta}$ matches the distribution for $\theta/2$ since the Haar phase

¹ The tolerance $t_{\theta;\alpha} \propto \sigma_{\theta;\alpha}$. The allowable tolerance specifies the phase uncertainty required to feasibly implement (or optimize) a unitary operator, and it may vary depending on the application.

ξ_{mn} is the CDF for $\theta_{mn}/2$. Compared to optimizations parametrized by θ_{mn} , optimizations parametrized by the Haar phase spend less time in places where the gradient $\frac{d\theta}{d\xi}$ is high, and more time in places where the gradient is low, thus finding Haar random unitaries efficiently.

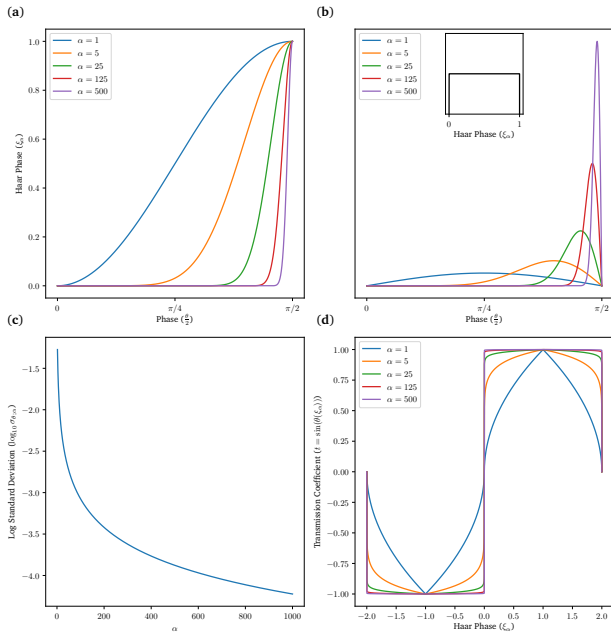


FIG. 2. (a) Plot of the relationship between ξ_α and θ . (b) We show that uniform distributions of ξ leads to lower standard deviation $\sigma_{\theta;\alpha}$ as α increases. (c) A plot of $\sigma_{\theta;\alpha}$ as α increases. Note that thermal crosstalk errors in thermal phase shifter implementations [6] make most RD meshes in the plotted range difficult to implement or optimize. (d) The reflection amplitude of an MZI component as a function of Haar phase of period 4. Exploding gradients occur in the rising and falling edges for large α . Vanishing gradients may also occur in the flat regions.

We also introduce “checkerboard plots” in Figure 3, which are spatial plots representing phase values in the mesh (the red dots in Figure 1 (c, d)). Similar plots are used in [18] to show the nontrivial reflectivity distribution throughout the rectangular mesh. For a Haar random unitary matrix, we find the exact values of θ_{mn} using the nullifying procedure in [9] and show that they compare to expected values $\theta_{mn}^{(0)} = \theta(0.5)$ (the zeroth order of the Taylor expansion around $\xi_\alpha = 0.5$). Note that the Haar phase ξ_{mn} parameters in the checkerboard are uniformly random. Uniformly random Haar phases can be used as an initialization procedure for on-chip unitary matrix optimizations.

As mentioned previously, optical transitions in the rectangular mesh for off-diagonal elements have fewer paths than those for the near-diagonal elements and thus are harder to control. If we parametrize each MZI at (m, n) by a uniformly distributed Haar phase ξ_{mn} instead of θ_{mn} , we achieve uniform control over these all unitary magnitudes. In theory, one might consider using

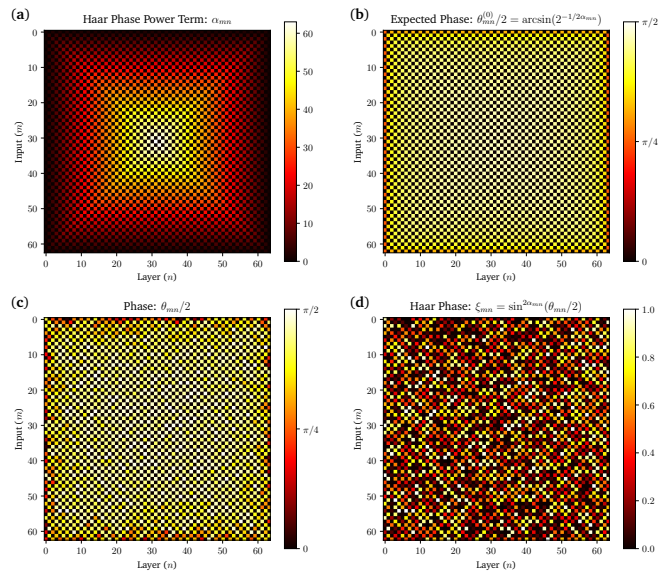


FIG. 3. The above “checkerboard plots” show the value of any tunable quantity that depends on m, n defined in the decompositions. (a) The Haar phase power term α_{mn} for $N = 64$. (b) Checkerboard plot of median zeroth order Taylor expansion term $\theta^{(0)}(\xi)$ for a Haar random mesh. (c) We randomly generate $U_{\Pi} \sim \text{CUE}(64)$ and compute RD using algorithm in [9]. (d) The Haar phase $\xi = \sin^{2\alpha_{mn}}(\theta_{mn}/2)$ for the RD mesh better displays the randomness.

the Haar phase rather than θ as the control parameter, but in practice, large numerical gradients present in the Haar phase leads to optimization instability (exploding gradients) or slow convergence (vanishing gradients), particularly for large Haar phase power terms α . In Figure 2(d), we demonstrate this exploding gradient in terms of the Haar phase-parametrized transmission coefficient of an MZI, $t(\xi_\alpha) = \sin(\theta(\xi_\alpha))$. We may use this expression to map transmissions for $\xi \in [0, 1]$ to transmissions for $\xi \in [-2, 2]$, just as one maps the trigonometric function $\sin\theta$ for $\theta/2 \in [0, \pi/2]$ to $\theta/2 \in [-\pi, \pi]$. The presence of a component-wise exploding gradient demonstrates that even if we could somehow implement a Haar phase-parametrized linear optical component², gradient-based optimizations would still be difficult and the components may be more prone to fabrication and voltage errors due to the switch-like behavior. These very problems motivate our coarse-grained and redundant mesh approaches.

IV. PHOTONIC MESH CANVAS

Conceptualizing the rectangular mesh as a “canvas” of passive and tunable beamsplitters allows experimen-

² The MZI phase control parameter, for example the voltage, could behave like a Haar phase.

tion with many architectures that converge to a unitary matrix significantly faster than RD. We find two modifications to rectangular decompositions that improve convergence performance that can be tested on a mesh canvas: redundant tunable layers (shown in green in Figure 4(a)) or nonlocalities (extra passive layers with $\theta/2 = \pi/2$, shown in gray in Figure 4(b)). We now proceed to discuss how nonlocalities can be added in a photonic mesh canvas.

A. Coarse-grained rectangular design

We define “coarse-graining” as introducing mesh nonlocalities using passive beamsplitters. These beamsplitters usually, but not necessarily, satisfy $\theta/2 = \pi/2$ or $\theta = 0$. Furthermore, these beamsplitters can introduce structured non-localities in the mesh by being placed at strategic nodes in the mesh. By shuffling outputs periodically in the rectangular mesh layers using coarse-graining, we more efficiently parametrize unitary space by increasing the tolerances $\sigma_{\theta_{mn}}$ and the uniformity of the number of paths for each input-output transition.

We will describe an example of coarse-graining that resamples the waveguides at regular intervals to significantly improve optimization performance. For simplicity³, assume $N = 2^K$ for some positive integer K . Define permutation operations P_k that allow inputs to interact with waveguides at most 2^k away for $k < K$. These rectangular permutation blocks can be implemented using a rectangular decomposition composed of MZIs with fixed phase shifts of $\theta/2 = \pi/2$ (the cross state), as shown in Figure 4. Equivalently, we could replace these crossed MZIs in this permutation block with crossing waveguides, which could result in a more compact structure. We also note that the P_k act as unitary operators in the mesh with the off-diagonal rectangular structure shown in Figure 4.

We now add permutation matrices $P_1 \cdots P_{K-1}$ into the middle of the rectangular decomposition. By inserting the rectangular permutation matrices between the commuting layers of Givens rotations in U_{Π} , we can still generate the unitary matrix, albeit with different parameters in the rectangular decomposition. The final expression for our desired efficient representation of unitary matrix U is:

$$U_{\Pi, \text{cgrd}}(\theta, \phi, \gamma) = \left(\prod_{k=1}^{K-1} M_k P_k \right) M_K, \quad (11)$$

$$M_k \equiv \prod_{n=(k-1)\lceil \frac{N}{K} \rceil}^{\min(k\lceil \frac{N}{K} \rceil, N)} U_{\Pi}^{(n)}(\theta_{mn}, \phi_{mn}).$$

³ If N is not a power of 2, then one might consider the following approximate design: $K = \lceil \log_2 N \rceil$. Define $b(K) = \sqrt[K]{N}$, and let each P_k have $\lceil b^k \rceil$ layers.

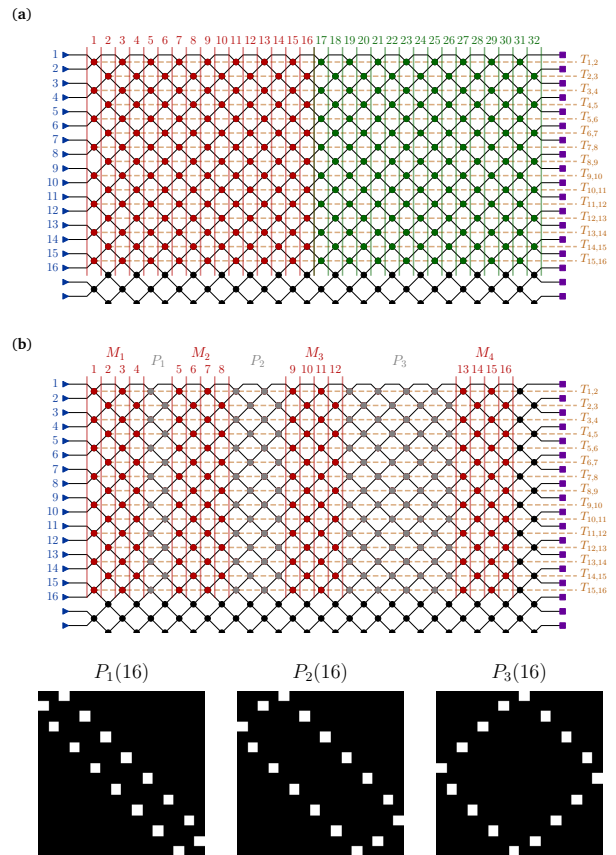


FIG. 4. (a) Embedding a 16×16 RD (red) inside of a 32-layer rectangular mesh canvas. Further layers may be set to be tunable (RRD layers, green) to significantly reduce convergence time. Note that black nodes correspond to bar state MZIs. (b) Embedding a 16×30 CGRD inside of a 32-layer rectangular mesh canvas. We implement the rectangular permutation layer using $\theta_{mn}/2 = \pi/2$ Givens rotations (gray). Below the mesh, we show rectangular permutation unitary matrices P_k for $N = 16$ (white pixels are 1, black pixels are 0).

There are two operations per block k : an $\lceil \frac{N}{K} \rceil$ -layer rectangular mesh which we abbreviate as M_k , and the rectangular permutation mesh P_k where block index $k \in [1 \cdots K - 1]$. This is demonstrated in Figure 4(b).

Compared to rectangular decomposition, a coarse-grained rectangular design (CGRD) mesh provides a much more efficient encoding of a Haar random unitary matrix. This higher efficiency can be thought of as a larger uncertainty for the phase parameter distribution necessary to achieve a Haar random matrix. Note that when the number of tunable layers is 1 in each block, our mesh architecture is similar to the Fast decomposition inspired by the Cooley-Tukey FFT algorithm, which despite its non-universality has already been shown to be more robust to loss and beamsplitter errors and have an efficient coverage of unitary space for Fourier quantum transformations [15]. This decomposition has also been successfully used in deep neural network simulations im-

plementing the copying memory task [23].

Although not an MZI mesh architecture, multi-plane light conversion (MPLC) successfully applies the non-local interference idea for efficient spatial mode multiplexing [26, 27]. In MPLC, alternating layers of transverse phase profiles and optical Fourier transforms (analogous to what our rectangular permutations accomplish) are applied to reshape input modes of light [26, 27]. A similar concept is used in unitary spatial mode manipulation, where stochastic optimization of deformable mirror settings allow for efficient mode conversion [28]. Thus, this idea of “efficient” unitary learning via a Fourier-inspired coarse-graining approach has precedent in contexts outside of photonic MZI meshes.

Because the P_k matrices do not depend on any training variables, these rectangular permutation layers can also be implemented as passive components on a nanophotonic chip (e.g. using waveguide crossings [29] or inverse-designed beamsplitters [30]). The advantage of implementing low-loss waveguide crossings is that we can optimize for random Haar matrices on a photonic chip significantly faster than an RD mesh without needing to double the size of the chip. However, any coarse-grained architecture using waveguide crossings is impossible to modify once fabricated. Ideally, one would test a coarse-grained architecture on a mesh canvas prior to fabrication using waveguide crossings.

An implementation strategy based on the “canvas” idea could be to simply double the number of layers of the RD mesh and implement $\theta_{mn}/2 = \pi/2$ phase shifts at the requisite layers, as shown in Figure 4(b), to form the rectangular permutation blocks. (The number of components in the canvas is equal to that of a network of double MZIs that allow for the perfecting of imperfect MZIs [19].)

Assuming a photonic chip of size N is built with minimal loss and fabrication errors, coarse-graining may technically be implemented for any $N' < N$, but is mostly useful for $N' \leq N/2$, as is the case in Figure 4(b). Furthermore, coarse-graining the necessary photonic circuitry to implement a unitary matrix of size N is not expensive since the size of the CGRD mesh is still $\mathcal{O}(N)$.

V. NUMERICAL EXPERIMENTS

A. Random matrix generation

Assuming $\theta_{mn} \sim \mathcal{U}(0, \pi)$ and $\phi_{mn}, \gamma_n \sim \mathcal{U}(0, 2\pi)$ (where \mathcal{U} denotes a uniform distribution), we define $\mathcal{U}_\Pi(N)$ as the distribution of phase-randomly generated unitary matrices. This distribution of matrices are expected to have non-zero elements only within a band of a given (band)width about the diagonal that decreases with circuit size N . We show this trend of “banded” matrices in Figure 5.

The set of Haar random matrices with dimension N is referred to as $\mathbf{CUE}(N)$ (circular unitary ensemble).

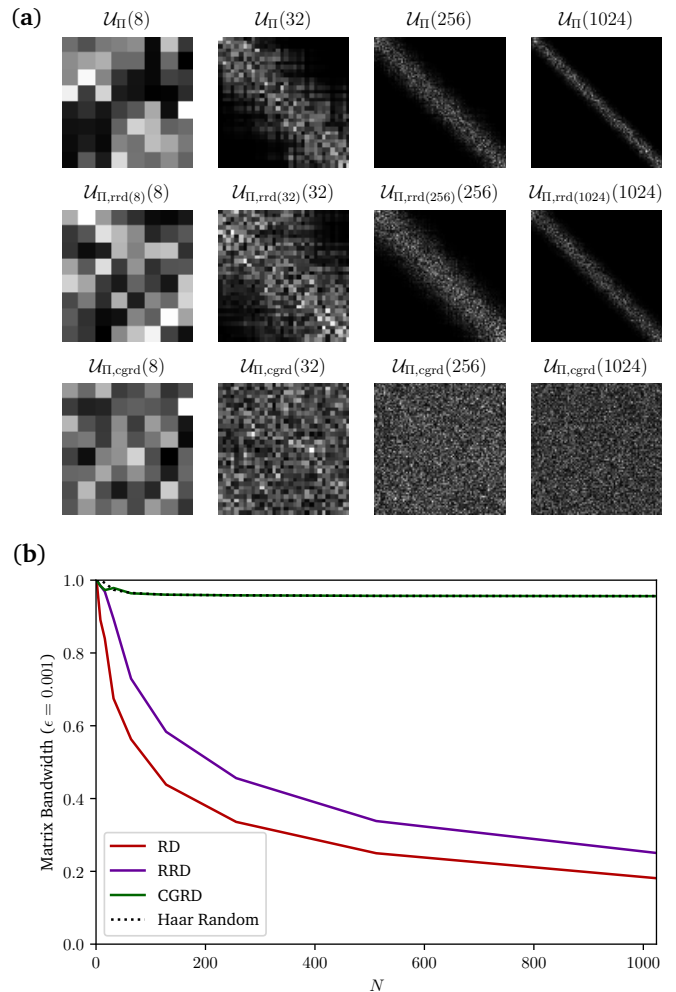


FIG. 5. (a) Plots of the absolute values of banded matrices resulting from $U_\Pi \sim \mathcal{U}_\Pi(N)$ and $U_{\Pi,rrd} \sim \mathcal{U}_{\Pi,rrd}(N, N)$, but not $U_{\Pi,cgrd} \sim \mathcal{U}_{\Pi,cgrd}(N)$. (b) CGRD meshes achieve the same bandwidths as the Haar random $\mathbf{CUE}(N)$ matrices, unlike RD meshes.

The distribution of phases θ_{mn} must follow the PDFs in Equation 9 to ensure that $U \sim \mathbf{CUE}(N)$. This finding tells us what the shape of our topological space is; by implementing a photonic mesh, we are working in a unitary space that is biased during the optimization towards banded unitary matrices. Even if we initialize the mesh with a Haar random matrix, we might expect (and we actually observe) off-diagonal elements to quickly go to zero as the RD mesh attempts to learn an unknown Haar random matrix.

We can measure the bandwidths of RD banded unitary matrices in numerical experiments. To accomplish this task, we randomly generate $U \sim \mathcal{U}_\Pi(N)$, $U \sim \mathcal{U}_{\Pi,cgrd}(N)$ (CGRD mesh with N tunable layers), and $U \sim \mathcal{U}_{\Pi,rrd}(\delta N)(N)$ (redundant mesh implementing $U \in \mathbf{U}(N)$ with $N + \delta N$ tunable layers).

We define the ϵ -bandwidth as the minimum number of elements whose absolute value squared sums up to

$(1 - \epsilon)N$. Note that our ϵ -bandwidth measurement is agnostic of the ordering of the inputs and outputs, and is therefore agnostic to any permutations that may be applied at the end of the decomposition. In photonic terms, if for example $\epsilon = 0.001$, we are measuring the average fraction of output waveguides over which 99.9% of the power is distributed given that light enters a single input of the decomposition mesh. Sampling from our random matrix distributions, we can observe the relationship between the matrix bandwidth and the dimension N for $\epsilon = 0.001$ as shown in Figure 5.

The higher-variance distribution of the parameters and the larger matrix band width in CGRD for Haar random matrices make it easier to train compared to RD despite the same number of tunable parameters. Furthermore, CGRD is less susceptible to random initialization than either RD or RRD for the simple reason that it has a larger matrix band width. Given a Haar-random initialization, however, we find that large band width is not necessary for fast optimization. Redundant rectangular decomposition (RRD) meshes make up for their banded random behavior with redundant parameters.

B. Simple unitary network

To better understand the search space topology of physical implementations of photonic unitary networks, we can run gradient optimizations that give us the necessary θ and ϕ update rules to learn any arbitrary unitary operation.

We showed evidence previously that the standard RD optimization favors banded unitary matrices. Our new CGRD method significantly improves upon the standard RD, with faster optimization convergence and more uniform errors.

To show this better convergence performance, we solve the following non-convex optimization problem of a simple unitary network (SUN).

$$\underset{\theta_{mn}, \phi_{mn}, \gamma_n}{\text{minimize}} \quad \frac{1}{2N} \left\| \hat{U}(\theta_{mn}, \phi_{mn}, \gamma_n) - U \right\|_F^2 \quad (12)$$

where the desired random unitary operation we want to learn is $U \sim \mathbf{CUE}(N)$, the estimated unitary matrix function \hat{U} maps N^2 angle parameters $\theta_{mn}, \phi_{mn}, \gamma_n$ to $U(N)$, and $\|\cdot\|_F$ corresponds to the Frobenius norm. This loss function is the infidelity $1 - \text{Tr}(U^\dagger \hat{U})/N$ used in [9, 18] assuming no loss. Since trigonometric functions parametrizing \hat{U} in Equation 12 are non-convex, we know that SUN is a non-convex problem. The non-convexity of SUN shows that even learning a single unitary transformation in a deep neural network is difficult and very highly dependent on initialization.

To train the SUN, we can generate random unit-norm complex vectors of size N and generate labels by multiplying them by the desired matrix U . Our training batch size is $2N$. The synthetic training data of

unit-norm complex vectors is therefore represented by $X \in \mathbb{C}^{2N \times N}$. The minibatch training loss is similar to the infidelity, $\mathcal{L}_{\text{train}} = \|\hat{X}U - XU\|_F^2$. The test set is the identity matrix I of size $N \times N$. The test loss, in accordance with the training loss definition, is the infidelity $\mathcal{L}_{\text{test}} = (1/2N)\|\hat{U} - U\|_F^2$, the SUN loss in Equation 12.

To initialize the SUN, we use Haar initialization, where we sample θ_{mn} from the PDF described in Section III. This initialization, which we highly recommend for any photonic mesh-based neural network application, allows for fast optimization performance as we show in Figure 6. If a mesh implementing SUN uses thermal phase shifters, thermal crosstalk may make such initializations difficult to achieve within reasonable tolerances for larger devices, especially RD meshes. This this could hurt performance of the meshes, but we find in our experiments that as long as the initialization is calibrated towards higher transmissivity $\theta_{mn}/2 \rightarrow \pi/2$, SUN can have reasonable convergence times, though not as good as when the phases are Haar-initialized. We find that a working strategy for initializing CGRD is to initialize each tunable block M_k as an independent mesh with $N/\log N$ layers since optimizing randomly initialized CGRD meshes led to simulated θ_{mn} variances corresponding to PDFs $\mathcal{P}(\theta; \alpha_{mn})$ for $\alpha_{mn} = \mathcal{O}(N/\log N)$, which we show in Appendix B.

The Adam gradient update [31] is preferable for the training of unitary networks on a conventional computer and may therefore also be more practical for physical on-chip optimizations of SUN [17]. This adaptive learning backpropagation approach is superior to other possible training approaches such as the finite difference method mentioned in past on-chip training proposals [6]. We choose a first-order adaptive update since quasi-Newton optimization methods such as BFGS used in [18] cannot be implemented physically as straightforwardly as first-order methods.

It is important to note that the SUN model can be directly implemented and tested on a photonic chip. The procedure in [17] physically measures $\partial \mathcal{L}_{\text{train}} / \partial \theta_{mn}$ for a photonic neural network with a single RD mesh. If these gradient measurements are stored during training, Adam updates (or any other viable adaptive updates) can be applied using successive gradient measurements for each tunable component in the mesh. Such a procedure requires minimal computation and can act as a physical test of the simulations we will now discuss.

C. Coarse-grained mesh optimization

We implement six different optimizations for $N = 128$ where we vary the model (CGRD or RD), the initialization (random θ_{mn} or Haar-initialized θ_{mn}), and photonic transmission error displacements ($\epsilon = 0$ or $\epsilon \sim \mathcal{U}(0.001, 0.011)$). We find that the order of performance goes as follows: RD-Random < RD-Photonic < RD-Ideal < CGRD-Random < CGRD-Photonic < CGRD-Ideal, which we define in the caption of Figure 6.

The random initialization has a much bigger effect on the RD mesh as compared to the CGRD mesh. The reason for the poor performance after random initialization, as compared to Haar initialization, has to do with the difficulty of finding α_{mn} during the optimization. As expected, the lower-tolerance phases in the RD mesh are much harder to learn after random initialization as compared to the higher-tolerance phases in the CGRD mesh, which are depicted in Appendix B. Furthermore, when introducing beamsplitter errors, several of the learned θ_{mn} were close to $\pi/2$ likely to account for unreachable transmissions ($|t|^2 > 1 - \epsilon_{mn}^2$) learned in the ideal meshes. There are much higher off-diagonal errors in the RD mesh (particularly near the corners where minimal learning occurs) as compared to the CGRD mesh, likely due to the reduced number of phase parameters for the off-diagonal elements. More comparisons and videos showing optimization time-evolutions are provided in Appendix B.

D. Redundant mesh optimization

Optimizing a rectangular or coarse-grained mesh may be viewed as a “full-capacity” optimization where only a minimum number of parameters are trainable (N^2 parameters for $U(N)$ parametrization), and the rest implement fixed phase shifts (usually $\theta_{mn}/2 = \pi/2, 0$).

The authors in [18] point out that using “underdetermined meshes” (number of tunable layers in the mesh greater than the number of inputs) can overcome photonic errors and restore fidelity in unitary construction algorithms. We show that such meshes with more than the single additional layer of beamsplitters suggested in [18] do well in photonic optimization. In particular, we see several orders of magnitude better convergence from the RRD MZI mesh compared to RD and CGRD as shown in Figure 7.

Like CGRD and RD meshes, the RRD mesh convergence time severely depends on the initialization, and like the RD mesh, random phase initialization results in poor convergence (not shown). There are two viable initializations. We initialized the RRD as a concatenation of a Haar-initialized N -layer mesh and a Haar-initialized δN -layer mesh. Second, redundant meshes can be initialized using the coarse-grained mesh initialization, which may help reduce some of the off-diagonal errors. We have not tried this initialization, but it is a worthwhile option to investigate.

For $N = 128$, the SUN convergence performance of the 256-layer RRD far exceeds that of RD and CGRD, achieving machine precision in the ideal case. Interestingly, adding just 32 layers to the mesh already exceeds the convergence performance of CGRD, and with just 16 layers we get almost identical performance. Redundant meshes are also robust to beamsplitter errors as shown in Appendix C.

One variant of redundancy is the singular value decomposition (SVD) mesh discussed in [5]. In SVD, we

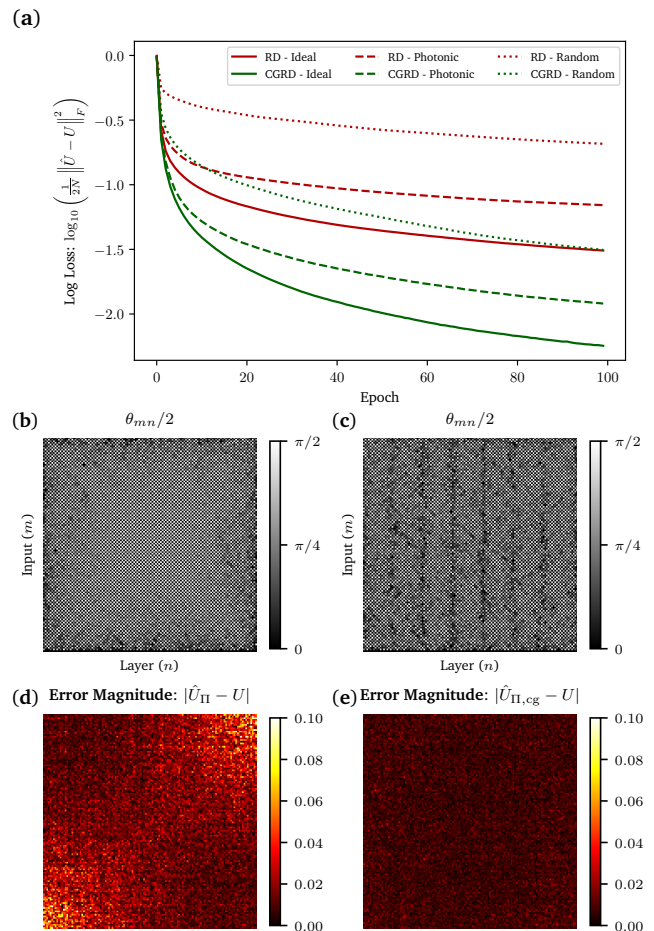


FIG. 6. A comparison of test loss (infidelity) for $N = 128$ between RD and CGRD for: 100 epochs (200 iterations per epoch), Adam update, learning rate of 0.025, batch size of 256, simulated in `tensorflow`. (a) Comparison of optimization performance. Random = Randomly initialized θ_{mn} ; Ideal = Haar random initialized θ_{mn} with $\epsilon = 0$; Photonic = Haar random initialized with $\epsilon \sim \mathcal{U}(0.001, 0.011)$. Optimized θ_{mn} for (b) RD-Ideal and (c) CGRD-Ideal. Optimized error magnitude spatial map for (d) RD-Ideal and (e) CGRD-Ideal. NOTE: by $|\cdot|$, we refer to the elementwise norm.

represent complex matrix $\hat{A} \in \mathbb{C}^M \times \mathbb{C}^N$ as $\hat{A} = \hat{U}\hat{\Sigma}\hat{V}^\dagger$, where $\hat{\Sigma}$ is a diagonal matrix implemented on-chip with $\min(M, N)$ single-mode gain or attenuating elements and \hat{U}, \hat{V}^\dagger are unitary matrices implemented on a photonic mesh canvas. While A has $2MN$ free parameters, any global optimization for a photonic SVD implementation using RD meshes can have at most $D = N(N - 1) + M(M - 1) + 2 \min(N, M) \geq 2MN$ free parameters, with equality when $M = N$. In the triangular architecture discussed in [5], the total complexity of parameters can be exactly $D = 2MN$ when setting a subset of the beamsplitters to bar state. In the case where the total number of singular values for A is $S < \min(M, N)$, we get $D = 2S(M + N - S)$ tunable elements. Additionally,

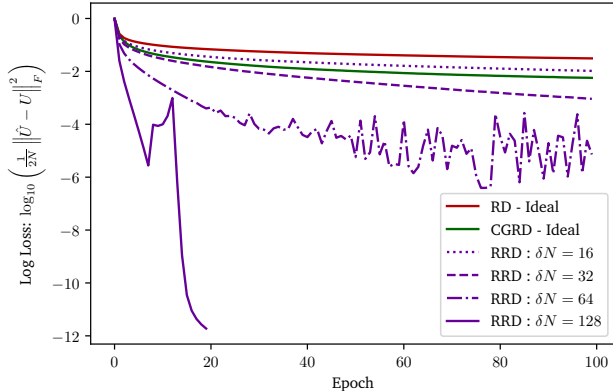


FIG. 7. A comparison of test loss (infidelity) in `tensorflow` for $N = 128$ between RRD, RD, CGRD for: 100 epochs (200 iterations per epoch), Adam update, learning rate of 0.05, batch size of 256. Ideal = Haar random initialized θ_{mn} with $\epsilon = 0$. δN is the additional layers added in RRD. We stopped the $\delta N = 128$ run early as it reached convergence within machine precision.

there is an “effective redundancy” in that some vectors in U, V are more important than others due to the singular values. Assuming a procedure similar to [17] can be used in presence of gains and losses, we find that CGRD converges about twice as fast as RD for an SVD model for $N = M = 64$, as shown in Appendix D.

VI. DISCUSSION

A. Haar phase parametrization

As we discussed in Section III, the Haar phase can be used to initialize the rectangular mesh. Haar phases for components that affect many inputs and outputs (i.e., components with large Haar phase power term α , which is $\mathcal{O}(N)$) are highly nonlinear functions of θ . Therefore, the resulting component-wise square wave behavior depicted in Figure 2 might be difficult to train or implement for large unitary matrices. We find that in simulation, attempts to directly optimize the Haar phase lead to numerical instability in RD meshes after just 20 Adam gradient updates. At the expense of universality and implementation flexibility, components might instead be biased towards high transmission to enable faster convergence. The Haar phases can also be used to initialize the optimization of an $N \times N$ decomposition mesh or directly dial Haar random matrices for boson sampling [2]. This initialization biases the search space of \hat{U}_{Π} to Haar random matrices $\mathbf{CUE}(N)$ as opposed to banded unitary matrices $\mathcal{U}_{\Pi}(N)$ that arise from uniform random phase settings. Even after this initialization, first-order optimizations of Haar random unitaries still have a difficult time optimizing off-diagonal elements of the unitary

matrix (a “vanishing gradient problem” in the context of machine learning), due to the bias of the optimization towards $\mathcal{U}_{\Pi}(N)$ (especially for large N).

In our numerical experiments in Section V, we assume that the control parameter for photonic meshes is error-free and linearly related to the phase. However, in many current phase shifter implementations, such as thermal phase shifters [6], the phase is a nonlinear function of the control parameter (i.e., the voltage). The voltage has a phase uncertainty that effectively behaves like a lower bound for achievable gradients during the optimization. In addition, like the Haar phase in our theory, the voltage acts as the CDF for phase shifter values θ_{mn} in the physical device, up to a normalization factor. Further simulation analysis parametrizing the SUN model by the voltage rather than the phase may more accurately model performance of practical on-chip training implementations. Particular attention needs to be given to phase uncertainty as a function of voltage, since the Haar random distribution of θ_{mn} has small variance for large N , as we showed in Figure 2(c). One might also consider strategically designing special transmissive MZIs in the center of the mesh that more closely mimic the distribution in Figure 2(b) and Figure 3, though such a design might limit the range of unitary sizes N one could implement on the chip. Instead, one might consider a variant of coarse-graining where MZIs near the mesh center are fixed at the “expected phases” shown in Figure 3(b), and tunable beamsplitter layers are added near the ends of the mesh to preserve the total number of parameters.

B. Machine learning with photonic meshes

For on-chip photonic deep learning platforms [6, 17], it also might suffice to make many of the layers an RD mesh. In intermediate photonic mesh layers, the RD mesh can effectively function as a discrete low pass filter transformation on inputs due to the banded distribution of unitary matrices typically learned by optimizing RD. Variants of RD might be valid candidates to complement recursive neural nets in finding local structure in sequences due to their locally interacting properties. For any sequence-learning task, such as natural language processing, complex sequence structure might not be as efficiently estimated by Haar random unitaries. An RD “tensor network,” on the other hand, may be able to model such complex structure well [32]. In previous unitary recursive neural net (uRNN) proposals [23, 33–35], RD unitary operations live in hidden layers and are succeeded by a modReLU nonlinearity. Instead, we propose using a single unitary matrix parametrized by RD or a singular value decomposition [5] to act over a full sequence as a translationally variant, locally connected tensor network. In such an optimization, one might consider eliminating some layers in the RD to reduce the number of parameters or coarse-graining the mesh to analyze the data over larger correlation length scales. These

coarse-graining ideas can be tested on a photonic mesh canvas prior to fabrication of more compact designs.

Ultimately, however, there are layers in the photonic neural network where we would need each input to access the output uniformly, i.e. to learn Haar random unitaries more easily. The rectangular mesh canvas allows us to do this via coarse-graining and redundancy. Our coarse-graining approach uses the same number of parameters as the rectangular mesh, resulting in uniform errors. Adding redundant layers to the mesh converges significantly faster than rectangular meshes due to increased parameter space. Despite this advantage, redundant meshes have the same non-locality (and thus error tolerance) problem as RD and may be prone to overfitting in photonic neural network applications due to a larger parameter space. The expense of additional photonic circuitry is minimal since smaller unitaries (of size $N' < N$) can always be implemented on a larger RD mesh.

We further propose the SUN model as a benchmark model for understanding how photonic circuitry may enhance matrix optimization. Using the SUN model, we can fairly compare how well meshes (with and without photonic errors) can learn a Haar random unitary matrix. The SUN test loss is the infidelity metric one uses to quantify the robustness of the mesh at implementing a given unitary matrix assuming no loss [15].

A theoretical analysis of the universality and the tolerances for CGRD meshes is still an open problem. We have not analyzed the random matrix theory or optimization performance of self-configuring cascaded binary tree [11] or triangular decompositions [8], which has slightly better beamsplitter tolerances than rectangular decompositions [15] and can be embedded in a rectangular mesh canvas. Self-configuring meshes also offer simple strategies for perfecting and calibrating component performance before configuration [19]. This calibration step may be valuable for initialization or for transfer learning in photonic neural networks.

VII. CONCLUSION

The scalability of universal unitary photonic meshes is limited by tolerances in phase shifters throughout the mesh network arising from the constraint of locally interacting components. As shown in Section III, the required error tolerance for each component scales with the total number of inputs and outputs affected by the component.

We have shown evidence in Section V that on-chip optimization of large Haar random unitary matrices in universal unitary photonic devices is limited by small MZI phase shifter tolerances. If the tolerance requirements are not met by the physical components, optimization algorithms will have trouble converging to an optimal

unitary operator. In our numerical experiments, convergence is generally not achieved if phase shifter values are initialized randomly. However uniformly initializing the Haar phase throughout the mesh as described in Section III can sufficiently bias the optimization towards Haar random unitary matrices to allow for convergence to the desired operator.

In Section IV, we propose the mesh canvas, a rectangular mesh of passive and tunable MZI components, to accelerate photonic matrix optimization. The mesh canvas can emulate scalable mesh architectures that compete with or enhance machine learning models. To evaluate the performance of these architectures, we use a simple unitary network (SUN) model and its fidelity metric. Our numerical experiments demonstrate that, even with simulated fabrication errors, the mesh canvas can learn unitaries faster when introducing non-localities (“coarse-graining”) or redundancies (extra tunable layers) with at most double the usual photonic circuitry.

The redundant rectangular decomposition (RRD) adds additional layers to the RD and improves optimization performance by a factor of 10^5 in our simulations. However, despite convergence advantages, redundant layers risk overfitting to training data due to the extra parameters, and the extent of this predicted overfitting warrants further investigation. By introducing non-localities in the mesh with a coarse-grained rectangular design (CGRD), we can increase the matrix bandwidth for random unitary matrix learning, thereby improving optimization performance by up to an order of magnitude without the need for extra parameters.

Further work is needed to investigate how fixed and tunable beamsplitters can be best organized in a mesh canvas to learn unknown unitary matrices. A hybrid architecture using coarse-graining and redundancy within a photonic mesh canvas using an intelligent initialization protocol may be promising for increasing the scalability⁴ and stability of universal photonic devices and their many classical and quantum applications.

ACKNOWLEDGEMENTS

This work was funded by the Air Force Office of Scientific Research, specifically for the Center for Energy-Efficient 3D Neuromorphic Nanocomputing (CEE3N²), Grant No. FA9550-181-1-0186.

Our unitary mesh code uses commuting layer definitions [33, 34]. We have modified and developed some of the code in [34] into a simulation framework, *neurophox*.

SP drafted the manuscript, conceptualized theory, wrote the optimization code, and designed figures and videos. BB wrote the rectangular decomposition code and Appendix E. OS and DM oversaw the work. SP, BB, OS, and DM revised the manuscript.

⁴ Photonic neural networks require circuit sizes up to $N = 1000$.

- [1] Markus Gräfe, Ren Heilmann, Maxime Lebugle, Diego Guzman-Silva, Armando Perez-Leija, and Alexander Szameit, “Integrated photonic quantum walks,” *Journal of Optics* (2016), 10.1088/2040-8978/18/10/103002.
- [2] Nicholas J. Russell, Levon Chakhmakhchyan, Jeremy L. O’Brien, and Anthony Laing, “Direct dialling of Haar random unitary matrices,” *New Journal of Physics* (2017), 10.1088/1367-2630/aa60ed.
- [3] Justin B. Spring, Benjamin J. Metcalf, Peter C. Humphreys, W. Steven Kolthammer, Xian Min Jin, Marco Barbieri, Animesh Datta, Nicholas Thomas-Peter, Nathan K. Langford, Dmytro Kundys, James C. Gates, Brian J. Smith, Peter G.R. Smith, and Ian A. Walmsley, “Boson sampling on a photonic chip,” *Science* (2013), 10.1126/science.1231692.
- [4] Andrea Annoni, Emanuele Guglielmi, Marco Carminati, Giorgio Ferrari, Marco Sampietro, David A.B. Miller, Andrea Melloni, and Francesco Morichetti, “Unscrambling light - Automatically undoing strong mixing between modes,” *Light: Science and Applications* **6** (2017), 10.1038/lsa.2017.110.
- [5] David A. B. Miller, “Self-configuring universal linear optical component [Invited],” *Photonics Research* **1**, 1 (2013).
- [6] Yichen Shen, Nicholas C. Harris, Scott Skirlo, Mihika Prabhu, Tom Baehr-Jones, Michael Hochberg, Xin Sun, Shijie Zhao, Hugo Larochelle, Dirk Englund, and Marin Soljačić, “Deep learning with coherent nanophotonic circuits,” *Nature Photonics* **11**, 441–446 (2017).
- [7] David A.B. Miller, “Establishing optimal wave communication channels automatically,” *Journal of Lightwave Technology* (2013), 10.1109/JLT.2013.2278809.
- [8] Michael Reck, Anton Zeilinger, Herbert J. Bernstein, and Philip Bertani, “Experimental realization of any discrete unitary operator,” *Physical Review Letters* (1994), 10.1103/PhysRevLett.73.58.
- [9] William R. Clements, Peter C. Humphreys, Benjamin J. Metcalf, W. Steven Kolthammer, and Ian A. Walsmsley, “Optimal design for universal multiport interferometers,” *Optica* **3**, 1460 (2016).
- [10] Nicholas C. Harris, Gregory R. Steinbrecher, Mihika Prabhu, Yoav Lahini, Jacob Mower, Darius Bunandar, Changchen Chen, Franco N.C. Wong, Tom Baehr-Jones, Michael Hochberg, Seth Lloyd, and Dirk Englund, “Quantum transport simulations in a programmable nanophotonic processor,” *Nature Photonics* **11**, 447–452 (2017).
- [11] David A. B. Miller, “Self-aligning universal beam coupler,” *Optics Express* (2013), 10.1364/OE.21.006360.
- [12] Daniel Perez, Ivana Gasulla, Jose Capmany, and Richard A. Soref, “Hexagonal waveguide mesh design for universal multiport interferometers,” in *2016 IEEE Photonics Conference, IPC 2016* (2017) pp. 285–286.
- [13] Daniel Pérez, Ivana Gasulla, Lee Crudgington, David J. Thomson, Ali Z. Khokhar, Ke Li, Wei Cao, Goran Z. Mashanovich, and Jos Capmany, “Silicon RF-Photonics Processor Reconfigurable Core,” in *European Conference on Optical Communication, ECOC* (2018).
- [14] Daniel Pérez, Ivana Gasulla, Lee Crudgington, David J. Thomson, Ali Z. Khokhar, Ke Li, Wei Cao, Goran Z. Mashanovich, and Jos Capmany, “Multipurpose silicon photonics signal processor core,” *Nature Communications* (2017), 10.1038/s41467-017-00714-1.
- [15] Fulvio Flamini, Nicol Spagnolo, Niko Viggianiello, Andrea Crespi, Roberto Osellame, and Fabio Sciarrino, “Benchmarking integrated linear-optical architectures for quantum information processing,” *Scientific Reports* **7**, 15133 (2017).
- [16] David A. B. Miller, “Setting up meshes of interferometers reversed local light interference method,” *Optics Express* (2017), 10.1364/OE.25.029233.
- [17] Tyler W Hughes, Momchil Minkov, Yu Shi, and Shan-hui Fan, “Training of photonic neural networks through in situ backpropagation and gradient measurement,” *Optica* **5**, 864–871 (2018).
- [18] Roel Burgwal, William R. Clements, Devin H. Smith, James C. Gates, W. Steven Kolthammer, Jelmer J. Renema, and Ian A. Walmsley, “Using an imperfect photonic network to implement random unitaries,” *Optics Express* **25**, 28236 (2017).
- [19] David A. B. Miller, “Perfect optics with imperfect components,” *Optica* **2**, 747 (2015).
- [20] C. M. Wilkes, X. Qiang, J. Wang, R. Santagati, S. Paesani, X. Zhou, D. A. B. Miller, G. D. Marshall, M. G. Thompson, and J. L. OBrien, “60dB high-extinction auto-configured MachZehnder interferometer,” *Optics Letters* (2016), 10.1364/OL.41.005318.
- [21] Maria Schuld and Nathan Killoran, “Quantum machine learning in feature Hilbert spaces,” (2018).
- [22] Maria Schuld, Alex Bocharov, Krysta Svore, and Nathan Wiebe, “Circuit-centric quantum classifiers,” (2018).
- [23] Li Jing, Yichen Shen, Tena Dubček, John Peurifoy, Scott Skirlo, Yann LeCun, Max Tegmark, and Marin Soljačić, “Tunable Efficient Unitary Neural Networks (EUNN) and their application to RNNs,” (2016), 10.1109/PHOSST.2017.8012714.
- [24] K. Zyczkowski and M. Kus, “Random unitary matrices,” *Journal of Physics A: General Physics* (1994), 10.1088/0305-4470/27/12/028.
- [25] Christoph Spengler, Marcus Huber, and Beatrix C. Hiesmayr, “Composite parameterization and Haar measure for all unitary and special unitary groups,” *Journal of Mathematical Physics* (2012), 10.1063/1.3672064.
- [26] Guillaume Labroille, Bertrand Denolle, Pu Jian, Jean Francois Morizur, Philippe Genevaux, and Nicolas Treps, “Efficient and mode selective spatial mode multiplexer based on multi-plane light conversion,” in *2014 IEEE Photonics Conference, IPC 2014* (2014).
- [27] Guillaume Labroille, Pu Jian, Nicolas Barré, Bertrand Denolle, and Jean-Francois Morizur, “Mode Selective 10-Mode Multiplexer based on Multi-Plane Light Conversion,” *Optical Fiber Communication Conference* (2016), 10.1364/OFC.2016.Th3E.5.
- [28] Jean-Francois Morizur, Lachlan Nicholls, Pu Jian, Seiji Armstrong, Nicolas Treps, Boris Hage, Magnus Hsu, Warwick Bowen, Jiri Janousek, and Hans-A. Bachor, “Programmable unitary spatial mode manipulation,” *Journal of the Optical Society of America A* **27**, 2524 (2010).
- [29] Yang Zhang, Amir Hosseini, Xiaochuan Xu, David Kwong, and Ray T. Chen, “Ultralow-loss silicon waveguide crossing using Bloch modes in index-engineered cas-

caded multimode-interference couplers,” *Optics Letters* (2013), 10.1364/OL.38.003608.

- [30] Alexander Y. Piggott, Jan Petykiewicz, Logan Su, and Jelena Vučković, “Fabrication-constrained nanophotonic inverse design,” *Scientific Reports* (2017), 10.1038/s41598-017-01939-2.
- [31] Diederik P Kingma and Jimmy Lei Ba, “Adam: A Method for Stochastic Optimization,” *International Conference on Learning Representations* (2015).
- [32] Vasily Pestun and Yiannis Vlassopoulos, “Tensor Network Language Model,” (2017).
- [33] Li Jing, Caglar Gulcehre, John Peurifoy, Yichen Shen, Max Tegmark, Marin Soljačić, and Yoshua Bengio, “Gated Orthogonal Recurrent Units: On Learning to Forget,” (2017).
- [34] Rumén Dangovski, Li Jing, and Marin Soljačić, “Rotational Unit of Memory,” (2017).
- [35] Martin Arjovsky, Amar Shah, and Yoshua Bengio, “Unitary evolution recurrent neural networks,” (2016).

Appendix A: Derivation of photonic unitary errors

Unitary matrices generated by lossless MZIs are prone to errors in beamsplitter fabrication. We introduce the error ϵ to our expression derived in Equation 1, which is twice the displacement in beamsplitter transmission power from 50 : 50. Hadamard gates with error ϵ are defined as $\hat{H}_\epsilon = \begin{bmatrix} \rho & \tau \\ \tau & -\rho \end{bmatrix}$ where ρ, τ are transmission and reflection amplitudes that result in slight variations from a 50 : 50 beamsplitter. We use this error definition since it is a measurable quantity in the chip; in fact, there are strategies to minimize ϵ directly [19]. The unitary matrix that we implement in presence of beamsplitter errors becomes

$$\begin{aligned} U_\epsilon &= \hat{H}_\epsilon \hat{R}_\theta \hat{H}_\epsilon \hat{R}_\phi \\ &= \begin{bmatrix} \rho & \tau \\ \tau & -\rho \end{bmatrix} \begin{bmatrix} e^{i\theta} & 0 \\ 0 & 1 \end{bmatrix} \begin{bmatrix} \rho & \tau \\ \tau & -\rho \end{bmatrix} \begin{bmatrix} e^{i\phi} & 0 \\ 0 & 1 \end{bmatrix} \\ &= \begin{bmatrix} r_\epsilon & -t_\epsilon^* \\ t_\epsilon & r_\epsilon^* \end{bmatrix}. \end{aligned} \quad (\text{A1})$$

Solving for t_ϵ in terms of t :

$$\begin{aligned} |t_\epsilon|^2 &= 4|\rho|^2|\tau|^2|t|^2 \\ &= 4|t|^2 \left(\frac{1}{2} + \frac{\epsilon}{2} \right) \left(\frac{1}{2} - \frac{\epsilon}{2} \right) \\ &= |t|^2(1 - \epsilon^2) \end{aligned} \quad (\text{A2})$$

Similarly, we can solve for r_ϵ :

$$|r_\epsilon|^2 = 1 - |t_\epsilon|^2 = |r|^2 + |t|^2\epsilon^2 \quad (\text{A3})$$

As we have shown in this paper, photonic errors ϵ as small as $\epsilon \sim 10^{-2}$ can have a significant impact on the optimization parameters and fidelity of unitary matrices.

Histogram: $\theta_{mn}/2$

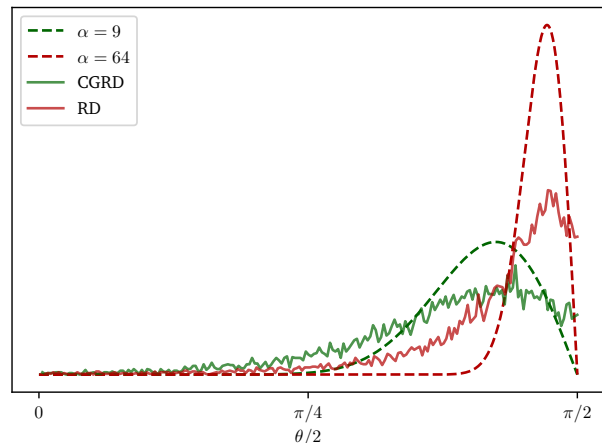


FIG. 8. Comparison of learned, normalized θ_{mn} distributions for $N = 128$ RD and CGRD with $\mathcal{P}(\theta/2; \alpha)$ PDFs for $\alpha = \frac{N}{2}$ and $\alpha = \lfloor \frac{N}{2 \log N} \rfloor$ respectively.

Appendix B: Comparison of on-chip training simulations

In Figure 9, we compare the performance for our simple unitary network experiment over our aforementioned conditions in Section V: RD and CGRD meshes for randomly initialized, Haar-initialized ideal, and Haar-initialized photonic optimization. Note that our simulated CGRD implementation uses the same layer definitions as defined in Equation 11 except the P_k with the most layers are in the center of the mesh, and the P_k with the fewest layers are near the inputs and outputs of the mesh. In Figure 4, P_2 and P_3 would be switched, and for $N = 128$, the order is $[P_2, P_4, P_6, P_5, P_3, P_1]$. Both our simulated CGRD implementation and the one in Equation 11 give improvements over RD, though the former performs slightly better. For each plot, we also have an associated video, showing how the parameter distributions, estimates, and errors vary during the course of the optimization, available online⁵.

The ϕ distributions are uniform as expected, but the θ checkerboard plots and distributions reveal evidence for our earlier claims for the behavior of α_{mn} for CGRD and RD meshes. Our simulations suggest that the standard deviation of $\sigma_{\theta_{mn}}$ (defined similarly as in Equation 10, except there is no Haar phase power term) correspond to distributions where $\alpha_{mn} = \mathcal{O}(N/\log N)$ for optimized CGRD matrices. This is ultimately a higher-entropy and higher-variance distribution than what is learned for RD where $\alpha_{mn} = \mathcal{O}(N)$. We show this comparison explicitly in Figure 8. As was also shown in the log-loss convergence comparison of Figure 6, the Haar phase initialization results in significantly better opti-

⁵ See <https://av.tib.eu/series/520/photonic+optimization>.

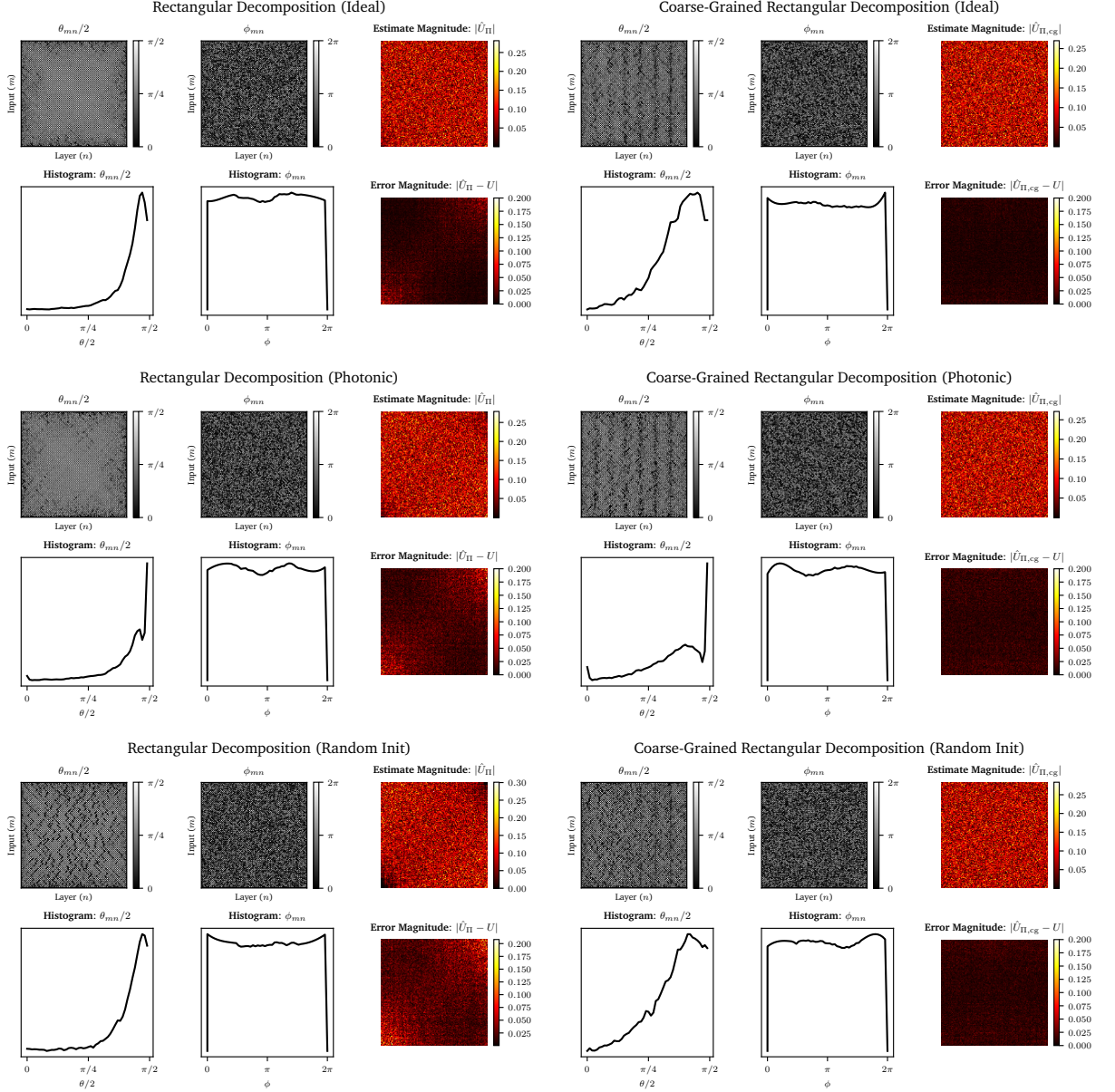


FIG. 9. Comparison of learned optimization weights after 20000 iterations for the Adam update at a learning rate of 0.005 for the simple unitary network. We consider two meshes: (1) rectangular mesh, and (2) coarse-grained rectangular mesh. We consider three conditions: (1) ideal (with Haar random unitary initialization), (2) photonic beamsplitter error displacement $\epsilon \sim \mathcal{U}(0.001, 0.011)$, (3) random initialization.

mization performance than random initialization. The RD Random checkerboard plot for θ_{mn} develops several “holes”—regions where $\theta_{mn}/2 \approx 0$ when it should be closer to $\pi/2$ —during the optimization. Likewise, the CGRD random checkerboard plot must learn the striped pattern present in the ideal CGRD checkerboard plot, though this process appears to be much faster than the randomly initialized RD mesh filling its holes. We have postulated in this paper off-diagonal errors are present due to the difficulty of finding θ in tight regions close to $\theta = \pi/2$, and these holes are numerical evidence.

An important observation for the meshes with photonic error is that there is a peak for θ_{mn} at $\pi/2$ in the θ_{mn} histograms. This is a consequence of the limitation to the reflectivity and transmission in each MZI due to beamsplitter fabrication error. This might occur when the mesh attempts to learn a MZI with transmission greater than $1 - \epsilon_{mn}^2$ (the maximum possible transmitted power for MZIs implementing $T_{m,m+1}$), in which case the optimization algorithm learns to set MZIs to their maximum transmission. This model learns to implement this maximum setting almost immediately (within the first

epoch or 200 iterations).

Appendix C: Introducing photonic errors in a redundant mesh

When photonic errors are added to the redundant mesh, specifically the 256-layer mesh, we observe a slight decrease in optimization performance, similar to what we observed for the RD and CGRD meshes as shown in Figure 10. This decrease in performance, however, is much less concerning considering that we still achieve a log loss of around -5, suggesting that RRD might be more robust to photonic errors even during on-chip optimization.

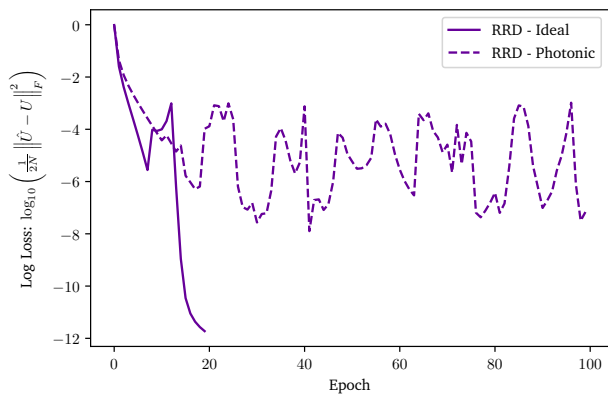


FIG. 10. A comparison of test loss for $N = 128$ between ideal and photonic 256-layer RRD for: 100 epochs (200 iterations per epoch), Adam update, learning rate of 0.05, batch size of 128, simulated in `tensorflow`.

Appendix D: Comparison of photonic singular value decomposition simulations

In order to compare the performance of standard RD and CGRD architectures in photonic neural networks, it may be prudent to compare the simulated performance of such architectures in the SVD configuration discussed in [5, 6]. Such architectures would allow one to perform arbitrary linear operations with a relatively small footprint, and may have some other useful dimensionality-reduction properties in machine learning contexts.

In our simulations, we investigate an SVD architecture for $A = U\Sigma V^\dagger$ for $A \in \mathbb{C}^M \times \mathbb{C}^N$ composed of $U \in \mathbb{C}^M \times \mathbb{C}^M$ and $V \in \mathbb{C}^N \times \mathbb{C}^N$. Note that such an architecture is redundant when $M \neq N$, so we focus on the simple case of $M = N = 64$.

We define our train and test loss analogous to the SUN model as

$$\begin{aligned} \mathcal{L}_{\text{test}} &= \frac{\|\hat{A} - A\|_F^2}{\|A\|_F^2} \\ \mathcal{L}_{\text{train}} &= \|X\hat{A} - XA\|_F^2, \end{aligned} \quad (\text{D1})$$

where $\hat{A} = \hat{U}\hat{\Sigma}\hat{V}^\dagger$ is defined in Section V.

We randomly generate $A \in \mathbb{C}^M \times \mathbb{C}^N$ by expressing $A_{jk} = a + ib$, where $a, b \sim \mathcal{N}(0, 1)$. The synthetic training batches of unit-norm complex vectors are represented by $X \in \mathbb{C}^{N \times 2N}$.

As shown in Figure 11, the CGRD mesh converges twice as fast as the RD mesh, and is more resilient to photonic errors and initialization compared to the RD mesh.

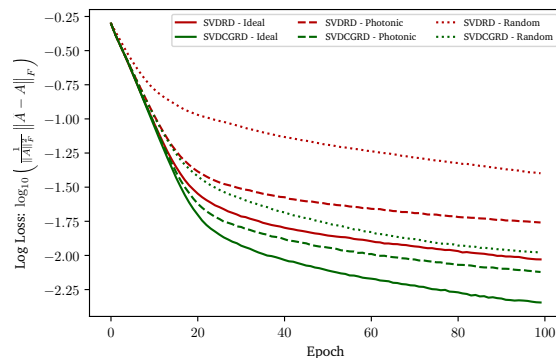


FIG. 11. A comparison of test loss for $N = 64$ between SVDRD and SVDCGRD for: 100 epochs (200 iterations per epoch), Adam update, learning rate of 0.05, batch size of 128, simulated in `tensorflow`. Random = Randomly initialized θ_{mn} ; Ideal = Haar random initialized θ_{mn} with $\epsilon = 0$; Photonic = Haar random initialized with $\epsilon \sim \mathcal{U}(0.001, 0.011)$.

Note that there is currently no straightforward way to implement the backpropagation procedure in [17] for the single-mode gain or attenuating components implementing singular values. However, in the case that such a procedure exists, our findings in Figure 11 show that CGRD will outperform RD in SVD implementations, and we postulate this may be the case because of their performance in SUN models.

Appendix E: An equivalent definition for the Haar phase power term α_{mn}

Let α_{mn} be the Haar phase power term for an MZI (“node”) at coordinates (m, n) in a local decomposition for an $N \times N$ unitary operator. We define the “row coordinate” m from the MZI’s operator $T_{m,m+1}$ coupling waveguides m and $m + 1$, and we define the “column coordinate” n to be $n = k + 1$, where k is the maximum number of operators applied to a reachable input (this is equivalent to the commuting layers definition in Figure 1). The reachable inputs I_{mn} are the subset of input waveguide modes affecting the immediate inputs of the MZI at m, n , and the reachable outputs O_{mn} are the subset of output modes affected by the immediate outputs of the MZI.

Following the definitions in Russell et al., in the triangular decomposition scheme, $\alpha_{mn} \equiv N - m$ [2], and in the rectangular decomposition scheme, $\alpha_{mn} \equiv \ell(m, n) + 1 - s_{mn}[n]$ where $\ell(m, n)$ is the number of nodes on the diagonal (measured along paths of constant $m+n$) containing a rotation parametrized by θ_{mn} , and s_{mn} is a sequence of decreasing odd integers $\ell(m, n) \geq n_{\text{odd}} \geq 1$, followed by increasing even integers $2 \leq n_{\text{even}} \leq \ell(m, n)$ [2]. We prove below that for both the triangular and rectangular decompositions, $\alpha_{mn} = |I_{mn}| + |O_{mn}| - N - 1$.

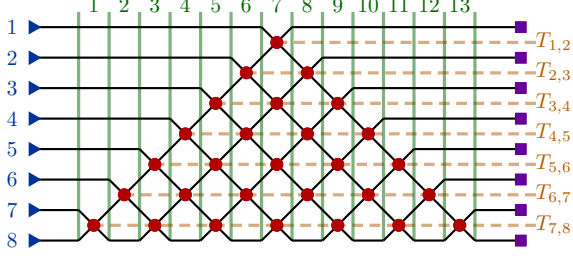


FIG. 12. Triangular decomposition for $N = 8$. Induction on m, n visits only nodes of the same parity, so two base cases are required.

Lemma 1. *In the triangular decomposition, $\alpha_{mn} = |I_{mn}| + |O_{mn}| - N - 1$.*

Proof. In the triangular decomposition (shown for $N = 8$ in Figure 12) $\alpha_{mn} \equiv N - m$, so we wish to show that $N - m = |I_{mn}| + |O_{mn}| - N - 1$, or:

$$2N + 1 = |I_{mn}| + |O_{mn}| + m. \quad (\text{E1})$$

Suppose Equation E1 holds for some arbitrary m', n' in the mesh, such that $2N + 1 = |I_{m'n'}| + |O_{m'n'}| + m'$. First, induct on m : if we take $m = m' + 2$ and $n = n'$, then $|I_{mn}| = |I_{m'n'}| - 1$ and $|O_{mn}| = |O_{m'n'}| - 1$. Next, induct on n : if we take $m = m'$ and $n = n' + 2$, then $|I_{mn}| = |I_{m'n'}| + 1$ and $|O_{mn}| = |O_{m'n'}| - 1$. In both cases, Equation E1 holds.

Traversals by 2 along m or n from a starting node can reach all nodes with the same parity of m and n , so we need two base cases. Consider the apex node at $m = 1$, $n = N - 1$ and one of its neighbors at $m = 2$, $n = N$. The former has $|I_{mn}| = |O_{mn}| = N$ and the latter has $|I_{mn}| = N$ and $|O_{mn}| = N - 1$. In both cases, Equation E1 is satisfied, so the lemma holds by induction. \square

Lemma 2. *In the rectangular decomposition, $\alpha_{mn} = |I_{mn}| + |O_{mn}| - N - 1$.*

Proof. In the rectangular decomposition, $\alpha_{mn} \equiv \ell(m, n) + 1 - s_{mn}[n]$. Define orthogonal axes x and y on the lattice such that for a node at (m, n) , traveling in the $+x$ direction gives the neighboring node at $(m + 1, n + 1)$ and traveling in the $+y$ direction gives the neighboring node at $(m - 1, n + 1)$. For even $\{\text{odd}\} N$, let the node at $(m, n) = (1, 1)$ have $x = 1$ and the node at $(m, n) = (N - 1, 1\{2\})$ have $y = 1$. Then there is a one-to-one mapping such that $(x, y) = (\frac{m+n}{2}, \frac{n-m}{2} + \lfloor \frac{N}{2} \rfloor)$ and it suffices to prove the lemma by induction in this diagonal basis.

Since $\ell(m, n)$ is defined to be the length of a diagonal along paths of constant $m + n$, it depends only on x , so we rewrite $\ell(m, n) \rightarrow \ell(x)$ explicitly:

$$\ell(x) = \begin{cases} 2x - 1 & x \leq \lfloor \frac{N}{2} \rfloor \\ 2(N - x) & x > \lfloor \frac{N}{2} \rfloor \end{cases}. \quad (\text{E2})$$

Similarly, since $s_{mn}[n]$ is enumerated along a diagonal, it depends only on y , and we convert $s_{mn}[n] \rightarrow s_x[y]$ from a sequence to an explicit lattice form:

$$s_x[y] = \begin{cases} 2(\lfloor \frac{N}{2} \rfloor - y) + 1 & y \leq \lfloor \frac{N}{2} \rfloor \\ 2(y - \lfloor \frac{N}{2} \rfloor) & y > \lfloor \frac{N}{2} \rfloor \end{cases}. \quad (\text{E3})$$

In this diagonal basis, we want to show that

$$\ell(x) + 1 - s_x[y] = |I_{xy}| + |O_{xy}| - N - 1. \quad (\text{E4})$$

There are two boundaries at $x, y = \lfloor \frac{N}{2} \rfloor$ which separate four quadrants that must be considered. We will induct on x and y within each quadrant, then induct on x or y across each of the two boundaries.

Suppose that Equation E4 holds for some arbitrary x', y' in the mesh, such that $\ell(x') + 1 - s_{x'}[y'] = |I_{x'y'}| + |O_{x'y'}| - N - 1$. First, we induct on x and y within each quadrant; the results are tabulated in Table E.

Note that in every case, $\ell(x) - s_x[y] - |I_{xy}| - |O_{xy}| = \ell(m, n) - s_{x'}[y'] - |I_{x'y'}| - |O_{x'y'}|$, so Equation E4 remains satisfied.

Next, we induct across the $x, y = \lfloor \frac{N}{2} \rfloor$ boundaries, shown in Table E. (Recall that $|I_{xy}| = |I_{x'y'}| + 0\{1\}$ denotes that $|I_{xy}| = |I_{x'y'}|$ for even N and $|I_{xy}| = |I_{x'y'}| + 1$ for odd N .)

As before, in every case, $\ell(x) - s_x[y] - |I_{xy}| - |O_{xy}| = \ell(m, n) - s_{x'}[y'] - |I_{x'y'}| - |O_{x'y'}|$, satisfying Equation E4.

Finally, note that the base case of the top left MZI at $(n, m) = (1, 1)$, $(x, y) = (1, \lfloor \frac{N}{2} \rfloor)$ holds, with $\ell(x) + 1 - s_x[y] = 1 = 2 + N - N - 1 = |I_{xy}| + |O_{xy}| - N - 1$. This completes the proof in the (x, y) basis, and since there is a one-to-one mapping between $(x, y) \leftrightarrow (m, n)$, $\alpha_{mn} = |I_{mn}| + |O_{mn}| - N - 1$ holds by induction. \square

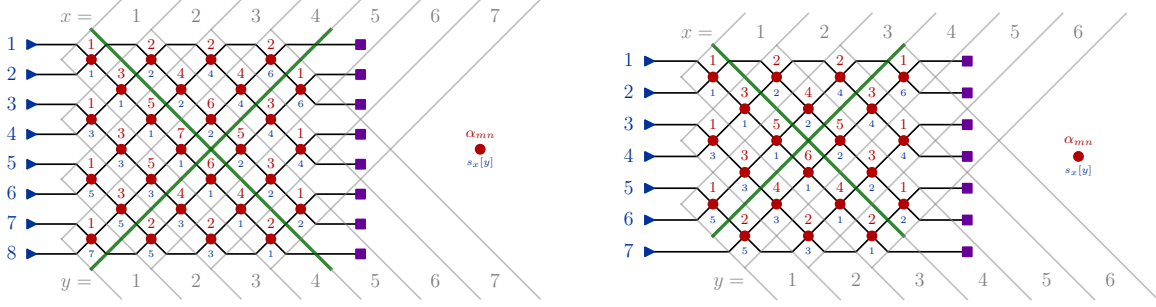


FIG. 13. Rectangular decomposition for even ($N = 8$) and odd ($N = 7$) meshes, showing the diagonal x, y basis. Values for α_{mn} are shown in red above each MZI, with values for $s_x[y]$ shown in blue below. The critical boundaries of $x, y = \lfloor \frac{N}{2} \rfloor$ separating the different quadrants are drawn in green. (Boundaries are offset for visual clarity.)

Quadrant	Induction	$\ell(x) = \dots$	$s_x[y] = \dots$	$ I_{xy} = \dots$	$ O_{xy} = \dots$
$x' \leq \lfloor \frac{N}{2} \rfloor, y' \leq \lfloor \frac{N}{2} \rfloor$	$x = x' - 1$	$\ell(m, n) - 2$	$s_{x'}[y']$	$ I_{x'y'} - 2$	$ O_{x'y'} $
	$y = y' - 1$	$\ell(m, n)$	$s_{x'}[y'] + 2$	$ I_{x'y'} - 2$	$ O_{x'y'} $
$x' \leq \lfloor \frac{N}{2} \rfloor, y' > \lfloor \frac{N}{2} \rfloor$	$x = x' - 1$	$\ell(m, n) - 2$	$s_{x'}[y']$	$ I_{x'y'} - 2$	$ O_{x'y'} $
	$y = y' + 1$	$\ell(m, n)$	$s_{x'}[y'] + 2$	$ I_{x'y'} $	$ O_{x'y'} - 2$
$x' > \lfloor \frac{N}{2} \rfloor, y' \leq \lfloor \frac{N}{2} \rfloor$	$x = x' + 1$	$\ell(m, n) - 2$	$s_{x'}[y']$	$ I_{x'y'} $	$ O_{x'y'} - 2$
	$y = y' - 1$	$\ell(m, n)$	$s_{x'}[y'] + 2$	$ I_{x'y'} - 2$	$ O_{x'y'} $
$x' > \lfloor \frac{N}{2} \rfloor, y' > \lfloor \frac{N}{2} \rfloor$	$x = x' + 1$	$\ell(m, n) - 2$	$s_{x'}[y']$	$ I_{x'y'} $	$ O_{x'y'} - 2$
	$y = y' + 1$	$\ell(m, n)$	$s_{x'}[y'] + 2$	$ I_{x'y'} $	$ O_{x'y'} - 2$

TABLE I. Induction on x and y within each of the quadrants in the mesh.

x'	y'	induction	$\ell(x) = \dots$	$s_x[y] = \dots$	$ I_{xy} = \dots$	$ O_{xy} = \dots$
$x' = \lfloor \frac{N}{2} \rfloor$	any	$x = x' + 1$	$\ell(m, n) - \{+\}1$	$s_{x'}[y']$	$ I_{x'y'} + 0\{1\}$	$ O_{x'y'} - 1\{0\}$
any	$y' = \lfloor \frac{N}{2} \rfloor$	$y = y' + 1$	$\ell(m, n)$	$s_{x'}[y'] + 1$	$ I_{x'y'} $	$ O_{x'y'} - 1$

TABLE II. Induction on x or y across each of the borders of $x, y = \lfloor \frac{N}{2} \rfloor$.